



**High Rates of Oxygen Reduction over a Vapor
Phase Polymerized PEDOT Electrode**

Bjorn Winther-Jensen, *et al.*

Science **321**, 671 (2008);

DOI: 10.1126/science.1159267

***The following resources related to this article are available online at
www.sciencemag.org (this information is current as of July 31, 2008):***

Updated information and services, including high-resolution figures, can be found in the online version of this article at:

<http://www.sciencemag.org/cgi/content/full/321/5889/671>

Supporting Online Material can be found at:

<http://www.sciencemag.org/cgi/content/full/321/5889/671/DC1>

This article **cites 28 articles**, 2 of which can be accessed for free:

<http://www.sciencemag.org/cgi/content/full/321/5889/671#otherarticles>

This article appears in the following **subject collections**:

Chemistry

<http://www.sciencemag.org/cgi/collection/chemistry>

Information about obtaining **reprints** of this article or about obtaining **permission to reproduce this article** in whole or in part can be found at:

<http://www.sciencemag.org/about/permissions.dtl>

cific angular momentum of the gas within radius r , and v_{Kep} is the Keplerian velocity at that radius.

Within a mass of $\sim 0.1 M_{\odot}$, two spiral arms rotated rapidly; the outer part (~ 0.05 to $0.1 M_{\odot}$) appeared nearly centrifugally supported, whereas the central part had gravitationally collapsed. The central core lost part of its angular momentum via gravitational torques exerted by nonaxisymmetric perturbations. The newly born protostar was supported by both thermal pressure and rotation. The overall velocity structure was characteristic of a collapsing gas with an initially slow rotation, as reported in previous studies of both protostellar and primordial star formation (19, 20).

A long-standing question is whether a primordial gas cloud such as that studied here experiences vigorous fragmentation by thermal instability during its evolution. In our simulation, a single small protostellar core formed first and the central part did not fragment into multiple objects before protostar formation. At all phases, the locally estimated growth time for isobaric perturbations was longer than, or only comparable to, the local dynamical time for collapse. Hence, the cloud core did not fragment by thermal instability, but instead its collapse accelerated. It has been suggested that the central part of primordial gas clouds may break up into smaller clumps during the subsequent accretion phase (20, 21). We examined a core fragmentation model of (19) by measuring Ωt_{dyn} , where Ω is the mean angular velocity and the local dynamical time $t_{\text{dyn}} = 1/[(4\pi G\rho)^{1/2}]$ (where G is the gravitational constant and ρ is the gas density). The central $\sim 0.01 M_{\odot}$ portion had a value of $\Omega t_{\text{dyn}} = 0.25$, which is large and close to the critical value for fragmentation. Thus, the formation of multiple stellar systems may be possible, although not very likely, during later accretion phases.

The instantaneous gas mass accretion rate at the time of protostar formation was as large as 0.01 to $0.1 M_{\odot}$ per year within the innermost $10 M_{\odot}$. If the gas in the inner portion accreted efficiently, the protostar would quickly grow to be as massive as $10 M_{\odot}$ within 1000 years (22). Even if multiple stellar seeds formed, there would be at least one main accreting protostar. A detailed protostellar calculation for a similarly large accretion rate predicts that the mass of the star when it lands on the main sequence will be $\sim 100 M_{\odot}$ (13, 23).

Feedback effects, in particular those from ionizing photons emitted by the protostar, work to evaporate the surrounding gas and to halt gas accretion. A semianalytic calculation including this radiative feedback and the effect of rotation shows that the final stellar mass can still be greater than a few tens of solar masses in a reasonable parameter space of the model (24). If instead mass accretion is unimpeded throughout the star's evolution, the final stellar mass can be very large, possibly exceeding a few hundred solar masses (22, 23). Such very massive stars ionize a large volume of the surrounding gas. Because of the different thermal evolution of an

initially ionized gas (25), second-generation primordial stars formed under such conditions are predicted to be several tens of solar masses (26, 27). Therefore, in either case, our model provides a viable scenario for the early chemical enrichment in the universe by massive primordial stars (6), which is necessary for the formation of later populations of ordinary stars.

The basic properties of the particular star-forming cloud we simulate, such as physical size and mass, are characteristic for cosmological primordial gas clouds, and the object is indeed similar in many aspects to those found in previous work (10, 11, 28). The final evolution of the central high-density part will likely be affected by its angular momentum content (20). However, because the bulk of the cloud core is assembled from material with low angular momentum (13), it generally has a slow initial spin, and thus the evolution of prestellar gas is expected to be similar to what is presented here. Our simulation thus offers a complete picture of how a primordial protostar may have formed from tiny cosmological density fluctuations. Primordial star formation for different cosmological models has been explored (29, 30). The particle properties of dark matter may be another important factor in star formation in the early universe.

References and Notes

1. X. Fan *et al.*, *Astron. J.* **125**, 1649 (2003).
2. M. Iye *et al.*, *Nature* **443**, 186 (2006).
3. F. Walter *et al.*, *Nature* **424**, 406 (2003).
4. N. Christlieb *et al.*, *Nature* **419**, 904 (2002).
5. A. Frebel *et al.*, *Nature* **434**, 871 (2005).
6. N. Iwamoto *et al.*, *Science* **309**, 451 (2005); published online 2 June 2005 (10.1126/science.1112997).
7. Y. Komiya *et al.*, *Astrophys. J.* **658**, 367 (2007).
8. D. N. Spergel *et al.*, *Astrophys. J.* **424**, 406 (2007).
9. V. Bromm, P. S. Coppi, R. B. Larson, *Astrophys. J.* **527**, L5 (1999).

10. T. Abel, G. L. Bryan, M. L. Norman, *Science* **295**, 93 (2002); published online 15 November 2001 (10.1126/science.1063991).
11. V. Bromm, P. S. Coppi, R. B. Larson, *Astrophys. J.* **564**, 23 (2002).
12. K. Omukai, R. Nishi, *Astrophys. J.* **508**, 141 (1998).
13. N. Yoshida, K. Omukai, L. Hernquist, T. Abel, *Astrophys. J.* **652**, 6 (2006).
14. See supporting material on Science Online.
15. T. Hanawa, T. Matsumoto, *Pub. Astron. Soc. Jpn.* **52**, 241 (2000).
16. K. Omukai, T. Tsuribe, R. Schneider, A. Ferrara, *Astrophys. J.* **626**, 627 (2005).
17. R. B. Larson, *Mon. Not. R. Astron. Soc.* **145**, 271 (1969).
18. E. Ripamonti, F. Haardt, A. Ferrara, M. Colpi, *Mon. Not. R. Astron. Soc.* **334**, 401 (2002).
19. T. Matsumoto, T. Hanawa, *Astrophys. J.* **595**, 913 (2003).
20. M. N. Machida, K. Omukai, T. Matsumoto, S. Inutsuka, *Astrophys. J.* **677**, 813 (2008).
21. P. C. Clark, S. C. O. Glover, R. S. Klessen, *Astrophys. J.* **672**, 757 (2008).
22. V. Bromm, A. Loeb, *New Astron.* **353**, 364 (2004).
23. K. Omukai, F. Palla, *Astrophys. J.* **589**, 677 (2003).
24. C. F. McKee, J. Tan, *Astrophys. J.* **681**, 771 (2008).
25. H. Uehara, S. Inutsuka, *Astrophys. J.* **531**, L91 (2000).
26. J. L. Johnson, V. Bromm, *Mon. Not. R. Astron. Soc.* **366**, 247 (2006).
27. N. Yoshida, K. Omukai, L. Hernquist, *Astrophys. J.* **667**, L117 (2007).
28. B. O'Shea, M. L. Norman, *Astrophys. J.* **654**, 66 (2007).
29. L. Gao, T. Theuns, *Science* **317**, 1527 (2007).
30. D. Spolyar, K. Freese, P. Gondolo, *Phys. Rev. Lett.* **100**, 051101 (2008).
31. We thank M. Machida and T. Matsumoto for fruitful discussions on gas cloud evolution. Supported by Grants-in-Aid for Young Scientists 17684008, 18740117, and 19047004 from the Ministry of Education, Culture, Science, and Technology of Japan and by the Mitsubishi Foundation (N.Y. and K.O.).

Supporting Online Material

www.sciencemag.org/cgi/content/full/321/5889/669/DC1
Materials and Methods
Figs. S1 and S2
References

9 May 2008; accepted 12 June 2008
10.1126/science.1160259

High Rates of Oxygen Reduction over a Vapor Phase–Polymerized PEDOT Electrode

Bjorn Winther-Jensen,* Orawan Winther-Jensen, Maria Forsyth, Douglas R. MacFarlane

The air electrode, which reduces oxygen (O_2), is a critical component in energy generation and storage applications such as fuel cells and metal/air batteries. The highest current densities are achieved with platinum (Pt), but in addition to its cost and scarcity, Pt particles in composite electrodes tend to be inactivated by contact with carbon monoxide (CO) or by agglomeration. We describe an air electrode based on a porous material coated with poly(3,4-ethylenedioxythiophene) (PEDOT), which acts as an O_2 reduction catalyst. Continuous operation for 1500 hours was demonstrated without material degradation or deterioration in performance. O_2 conversion rates were comparable with those of Pt-catalyzed electrodes of the same geometry, and the electrode was not sensitive to CO. Operation was demonstrated as an air electrode and as a dissolved O_2 electrode in aqueous solution.

Both fuel-cell technology for power generation and metal-air batteries for energy storage require an efficient electrode for O_2 reduction. Such air electrodes are usually a Pt

catalyst embedded in a porous carbon electrode. Despite having a high current density suitable for high-power applications such as vehicle drive systems (1–4), a number of issues with these elec-

trodes may ultimately limit the use and lifetime of the fuel cell or the storage battery, despite recent improvements (5, 6). For example, the cost of the Pt alone in a polymer membrane fuel cell for a small 100-kW passenger vehicle is substantially greater (at March 2008 prices) than the current cost of an entire 100-kW gasoline engine (7). Several technical issues also arise with the use of Pt catalysts. The Pt particles present in the composite electrode are not fixed in place, and a well-known drift phenomenon (8) by which the particles diffuse and agglomerate over time ultimately diminishes the performance of the fuel cell. Further, Pt is very sensitive to deactivation in the presence of CO, either in the air supply or as a by-product from the use of methanol in the direct methanol fuel cell (9–13).

Other metallic electrode materials, such as cobalt and Ru/Pt alloys (14, 15), have been explored to overcome some of these problems, but in all cases one or more of the issues remain. In particular, the sensitivity to CO is a particularly difficult problem to overcome. In this work, we have developed a Pt-free air electrode based on a nanoporous, intrinsically conductive polymer (ICP) multilayer structure that offers performance similar to that of Pt-catalyzed electrodes under parallel testing. Because the material is homogeneous, the drift issue is avoided and, being nonmetallic, the catalyst is not sensitive to CO poisoning.

The use of ICPs for catalytic electrodes was investigated early in the history of conducting polymer research and applications. However, success was limited by low conductivity and efficiency, and the instability of the ICP in the environment required for the catalysis (16–18). By incorporation of traditional catalytic centers such as Pt into ICPs, a range of catalytic electrodes have been reported (14, 19, 20), but these materials all suffer from many of the same problems as the Pt-C electrode. Recently, the development of chemical polymerization [in particular, a process known as vapor phase polymerization (VPP)] and “designed” ICP derivatives has produced materials with high conductivity, improved ordering and stability, and controllable porosity at the nanoscale (21–24). These properties improve the potential of these materials for electrocatalytic applications. Previous studies of PEDOT (25) have not been able to demonstrate catalysis of oxygen reduction; however, the improved thin-film properties obtained via VPP prompted us to reexamine its potential as an electrocatalytic material.

One of the key features of an air electrode is that it must establish a high-surface area boundary between the three active phases: air, the electrolyte, and the catalyst/conductor. To achieve this three-phase interface, we coated a PEDOT electro-active layer onto one side of a hydrophobic, porous membrane (Goretx). The procedure

developed here involves plasma polymerization of a binding layer to the polytetrafluoroethylene (PTFE) membrane, followed by VPP of the 3,4-ethylenedioxythiophene monomer to form the PEDOT conducting polymer (see fig. S1 for further details).

A schematic of the cross-sectional structure of the electrode in Fig. 1A shows the intended three-phase interface in the circled region. The designed structure allows access of the air stream from one side of the electrode to a high-surface area, electrochemically active layer of the PEDOT, which is simultaneously in contact with the electrolyte. The Goretx membrane provides a good, although not entirely optimized, starting point because it is highly porous at the micrometer level and, being hydrophobic, does not allow penetration of the aqueous electrolyte into the pores of the membrane. Because the electrical conductivity of PEDOT is still not high enough to provide a low-resistance path to the external circuit, a more electrically conductive underlayer was used. Coating one face of this membrane with a ~40-nm layer of gold provided the conductor layer without altering the structure of the membrane (Fig. 1B). In the next stage, a 400-nm PEDOT layer is created on one side by VPP (Fig. 1C). The structure of the underlying membrane is still visible after these deposition steps, which indicates that the three-phase boundary has been obtained over a substantial fraction of the membrane. An image of the cross-sections of the complete membrane assembly (Fig. 1D) shows the thin PEDOT layer on the surface of the structure.

From the thickness measurements, the mass of the PEDOT can be determined to be 0.05 mg/cm² for the optimum layer for this particular Goretx

membrane; this optimal thickness will change with pore size and shape of the membrane.

The Goretx/PEDOT electrode was subjected to testing as an air electrode at various pH levels and potentials in a cell that allowed direct contact with air from one side and electrolyte from the other (see fig. S2 for detailed experimental setup). The air reduction current under standard conditions (Fig. 2) shows that the electrode performs well over a wide pH range. The PEDOT membrane provides substantial oxygen reduction current densities at all of the pH conditions studied with the potential of onset of the reduction currents shifting as a function of pH in the expected way. To demonstrate that the underlying gold layer was not actively involved in the catalytic process, we conducted a separate experiment (fig. S3) using a Goretx membrane coated only with gold; this electrode produced substantially lower currents.

Continuous operation in air was achieved at -0.3 V versus saturated calomel electrode (SCE) for more than 1500 hours at pH = 1; 3 A·hour/cm² of charge was passed during this test. Testing of the electrochemical characteristics of the electrode after 1500 hours showed no change as a result of this period of operation (fig. S4).

Electrodes were constructed with PEDOT thicknesses ranging from around 40 to 1300 nm. It appears that the 400-nm coating shown in Figs. 1 and 2 is nearly optimal for this membrane pore size. When thicker coatings are applied, the diffusion of species, either in the electrolyte, or of oxygen through the PEDOT, becomes limiting and leads to lower currents.

For comparison purposes, we created a Pt-catalyzed electrode by depositing a 45-nm Pt

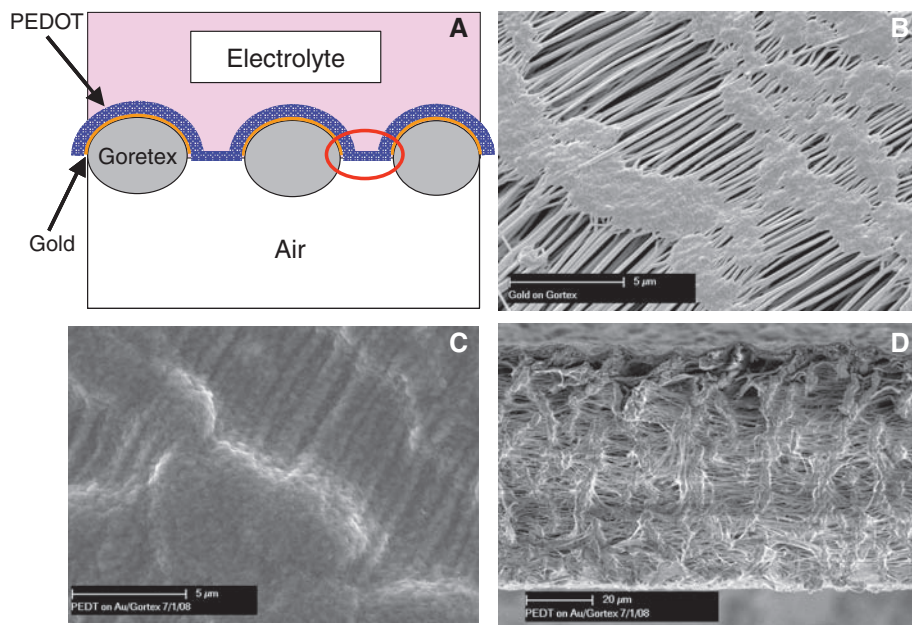
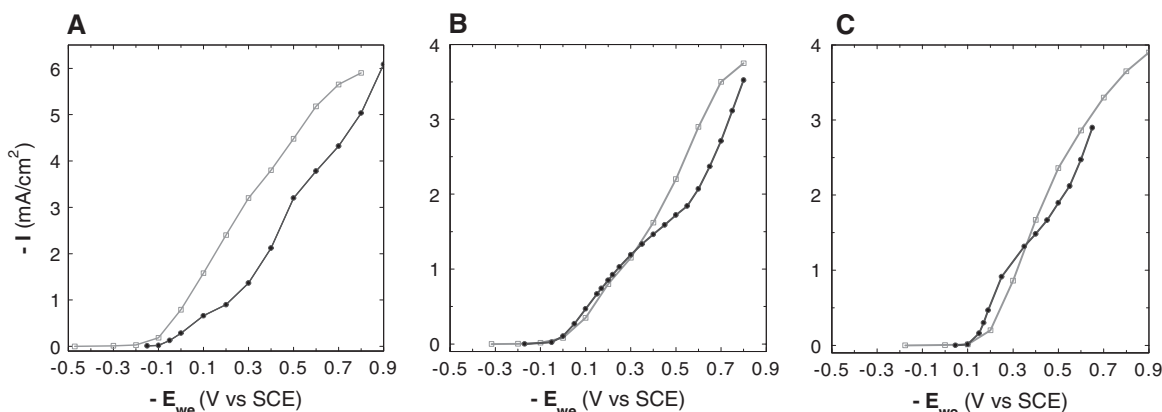


Fig. 1. (A) Schematic representation of the PEDOT/Goretx air electrode. (B to D) Scanning electron micrograph images: (B) The Goretx membrane coated with gold. Scale bar, 5 μm. (C) The PEDOT/Goretx structure. Scale bar, 5 μm. (D) Cross-section of the electrode with thickness measurements of the PEDOT layer. Scale bar, 20 μm.

Australian Centre for Electromaterials Science, Monash University, Clayton, Victoria 3800, Australia.

*To whom correspondence should be addressed. E-mail: bjorn.winther-jensen@eng.monash.edu.au

Fig. 2. Steady-state measurements (each point after 1 hour of continuous operation) of the conversion current versus potential at different pH values (black line: 400-nm PEDOT/Goretex; gray line: 45-nm Pt/Goretex). (A) pH 1, (B) pH 7, and (C) pH 13 for oxygen reduction from air.



layer onto the Au layer. The magnitudes of the conversion currents delivered by the PEDOT electrode are comparable to those of Pt for the same geometrical (membrane) area (Fig. 2). At pH 1, the Pt seems to perform better than the PEDOT electrode by a factor of ~ 2 , whereas at pH 7 and pH 13, the conversion currents are similar. The active surface area is actually considerably higher in the Pt case, because of the pore-filling effect of the thicker PEDOT layer in the Goretex membrane. It is also interesting that, although the thicknesses are different for the Pt (45 nm) and PEDOT (400 nm) layers, the difference in their densities (21.1 g/cm^3 for Pt and $\sim 1.2 \text{ g/cm}^3$ for PEDOT) means that the mass loading of active material is actually lower in the PEDOT case by a factor of ~ 2 . The electrocatalytic performance of the PEDOT material (up to $\sim 0.2 \text{ A/mg}$) is also similar to that of other recently reported cobalt-based materials (14).

The highest room-temperature current density observed with the membranes described here is $\sim 6 \text{ mA/cm}^2$. This value is sufficient for some metal/air batteries and a number of fuel-cell technologies including small direct methanol fuel cells, micro fuel cells, and the various biofuel cell concepts (9, 26). Higher-current density fuel-cell application of the PEDOT electrocatalyst concept would require extension of the three-phase interface into a thicker membrane structure.

The performance of the PEDOT and Pt-based assemblies is compared in Fig. 3A for different levels of CO contamination in the air supply; the PEDOT electrode is not affected, whereas the Pt electrode is poisoned very rapidly under identical conditions. The formation of carbonyl complexes of Pt at the surface that poisons its activity is unlikely with PEDOT. The effect of oxygen partial pressure in the gas supply (air = 20%) (Fig. 3B) demonstrates that the electrode is capable of even higher currents than are generated in air and that no limit related to processes within the PEDOT is being reached over the range of oxygen contents probed.

In a similar series of tests, the sensitivity of the electrode to the presence of methanol in the electrolyte was examined. Methanol crossover from the anode to the cathode is a major issue in the direct methanol fuel cell. The oxidation of

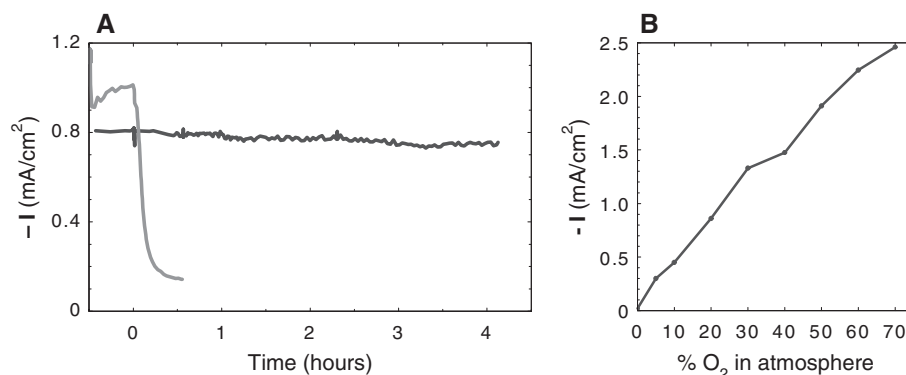
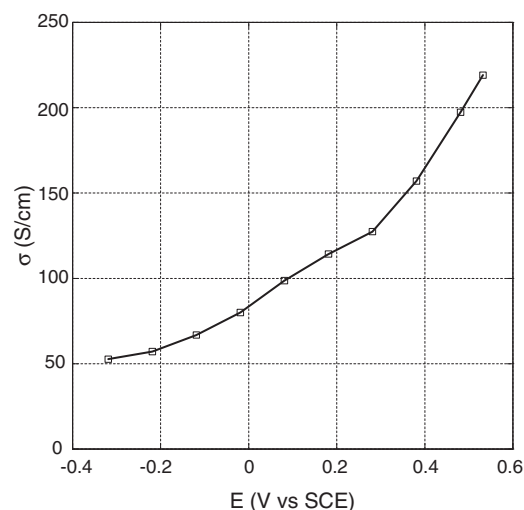


Fig. 3. Response of the PEDOT air electrode (black line) to different gas supplies (-0.3 V versus SCE, 0.1 M phosphate buffer, pH 7). (A) Current versus time in air contaminated by 10% CO compared to a similar Pt-catalyzed electrode (gray line). (B) Current as a function of oxygen content in the gas supply.

Fig. 4. Conductivity (σ) versus potential (E): Conductivity in PEDOT air electrode (0.1 M phosphate buffer, pH 7).



methanol is seen to be a competitive reaction to O_2 reduction on the cathode side (9). In the present work, a 1% addition of methanol was found to decrease the steady-state current at -0.3 V versus SCE by 20%, at which point the current again reached a steady value. Removal of the methanol brought the current back to its original value, indicating that no permanent damage to the electrode had been caused.

Further insight into the mechanism of the processes taking place in these PEDOT electrode

assemblies is provided by Fig. 4, which shows the electronic conductivity of the membrane as a function of the applied potential in an aqueous system. PEDOT in the absence of O_2 adopts a variable state of oxidation as a function of potential between about -0.5 to $+0.5 \text{ V}$ versus Ag/AgCl in aqueous solution (fig. S5). It is transformed from a low-conductivity material in its reduced state to a highly conductive material in its fully oxidized state. Operating the PEDOT air electrode at various potentials shows a conductiv-

ity profile with much higher conductivity at lower potentials (Fig. 4) compared to PEDOT in the absence of air (fig. S5), indicating that the PEDOT is reaching a steady-state oxidation level according to the applied potential, which is greater in the presence of air. The mechanism of the air reduction electrocatalysis likely involves a redox cycling process where the PEDOT, which naturally rests in an oxidized form, is momentarily reduced by the action of the electrochemical cell. An O₂ molecule then absorbs onto the surface of the PEDOT and rapidly reoxidizes the PEDOT to its preferred oxidized state and is itself reduced in the process. The role of the counterion in this mechanism, if any, is still unclear.

Given the similarity between the Pt and PEDOT responses in Fig. 2, it seems likely that the O₂ reduction proceeds via the four-electron pathway as it does on Pt, because there is no sign of an additional process that might indicate a contribution from H₂O₂ formation. Further investigation of the type described by Halseid *et al.* (27) is under way to probe the selectivity with respect to the four-electron pathway. Recent reports (28) describe efficient iron-loaded graphite catalysts for oxygen reduction. Given the very low Fe loadings involved, we cannot exclude the possibility of a role for residual Fe, at levels below the limit of x-ray photoelectron spectroscopy detection, in the mechanism reported here. However, iron-based catalytic centers would normally be expected to show signs of poisoning in the presence of CO; the resistance to CO poisoning seen here (Fig. 3) thus suggests that iron centers do not play a notable role.

A laboratory Zn/air battery was also constructed based on this PEDOT air-electrode assembly and a 1 M KOH electrolyte. An open-circuit voltage of

1.44 V was measured, comparable with other examples of this cell (29, 30). Discharge characteristics (fig. S6) as a function of current density and over a 48-hour continuous test were superior to similar devices constructed with a Pt/GoreTex air electrode.

The electrode described here provides only a partial solution to some of the problems with the use of Pt discussed in the introduction, because Pt is also used in the anode (fuel) electrode in the fuel cell. However, the fundamental mode of catalysis at work in the present materials may be able to be extended to other reactions, such as the hydrogen oxidation reaction, by careful choice of the ICP. ICPs can be successfully used as a substitute for Pt in dye-sensitized solar cells for the I⁻/I₃⁻ redox reaction (31). Thus, the development of the gas-ICP-electrolyte three-phase interface electrode reported here may provide a platform for a new generation of metal-free electrocatalysts.

References and Notes

1. T. Teratani, R. Mizutani, K. Yamamoto, T. Ane-gawa, *IEEJ Trans. Electr. Electron. Eng.* **3**, 162 (2008).
2. P. Agnolucci, *Int. J. Hydrogen Energy* **32**, 3526 (2007).
3. E. Pucher, A. Sekanina, *Elektrotechnik und Informationstechnik* **123**, 410 (2006).
4. K. Jorgensen, *Utilities Policy* **16**, 72 (2008).
5. V. R. Stamenkovic *et al.*, *Science* **315**, 493 (2007).
6. J. Zhang, K. Sasaki, E. Sutter, R. R. Adzic, *Science* **315**, 220 (2007).
7. University of Houston, "Fuel Cells Gearing Up To Power Auto Industry," *ScienceDaily*, 31 October 2007, retrieved 14 April 2008; www.sciencedaily.com/releases/2007/10/071030121117.htm.
8. X. Yu, S. Ye, *J. Power Sources* **172**, 145 (2007).
9. A. S. Arico, S. Srinivasan, V. Antonucci, *Fuel Cells* **1**, 133 (2001).
10. D. J. Ham, Y. K. Kim, S. H. Han, J. S. Lee, *Catal. Today* **132**, 117 (2008).
11. M. Winter, R. J. Brodd, *Chem. Rev.* **104**, 4245 (2004).

12. R. Liu *et al.*, *J. Phys. Chem. B* **104**, 3518 (2000).
13. J. S. Lee, S. Locatelli, S. T. Oyama, M. Boudart, *J. Catal.* **125**, 157 (1990).
14. R. Bashyam, P. Zelenay, *Nature* **443**, 63 (2006).
15. A. Garsuch *et al.*, *J. Electrochem. Soc.* **155**, B236 (2008).
16. R. C. M. Jakobs, L. J. Janssen, E. Barendrecht, *Electrochim. Acta* **30**, 1313 (1985).
17. N. F. Atta *et al.*, *J. Chem. Soc. Chem. Commun.*, 1347 (1990).
18. M. Somasundrum, J. V. Bannister, *J. Chem. Soc. Chem. Commun.*, 1629 (1993).
19. M. C. Lefebvre, Z. Qi, P. G. Pickup, *J. Electrochem. Soc.* **146**, 2054 (1999).
20. G. Tourillon, F. Garnier, *J. Phys. Chem.* **88**, 5281 (1984).
21. B. Winther-Jensen, K. West, *Macromolecules* **37**, 4538 (2004).
22. D. M. de Leeuw, P. A. Kraakman, P. F. G. Bongaerts, C. M. J. Mutsaers, D. B. M. Klaassen, *Synth. Met.* **66**, 263 (1994).
23. B. Winther-Jensen *et al.*, *Org. Electron.* **8**, 796 (2007).
24. B. Winther-Jensen *et al.*, *Polymer* **49**, 481 (2008).
25. V. Khomenko, V. Barsulov, A. Katashinski, *Electrochim. Acta* **50**, 1675 (2005).
26. D. Ivnitski, B. Branch, P. Atanassov, C. Appleby, *Electrochem. Commun.* **8**, 1204 (2006).
27. R. Halseid, M. Heinen, Z. Jusys, R. J. Behm, *J. Power Sources* **176**, 435 (2008).
28. E. Proietti, S. Ruggeri, J. P. Dodelet, *J. Electrochem. Soc.* **155**, B340 (2008).
29. A. A. Mohamad, *J. Power Sources* **159**, 752 (2006).
30. W. K. Chao, C. M. Lee, S. Y. Shieu, C. C. Chou, F. S. Shieu, *J. Power Sources* **177**, 637 (2008).
31. Y. Saito, W. Kubo, T. Kitamura, Y. Wada, S. Yanagida, *J. Photochem. Photobiol. Chem.* **164**, 153 (2004).
32. Funding of this work by the Australian Research Council (ARC) Centre of Excellence in Electromaterials Science is gratefully acknowledged, as is ARC Fellowship support for B.W.-J. (Australian Postdoctoral Fellowship) and D.R.M. (Federation Fellowship).

Supporting Online Material

www.sciencemag.org/cgi/content/full/321/5889/671/DC1
Materials and Methods
Figs. S1 to S6
References

17 April 2008; accepted 23 June 2008
10.1126/science.1159267

Structures of Neutral Au₇, Au₁₉, and Au₂₀ Clusters in the Gas Phase

Philipp Gruene,¹ David M. Rayner,² Britta Redlich,³ Alexander F. G. van der Meer,³ Jonathan T. Lyon,¹ Gerard Meijer,¹ André Fielicke^{1*}

The catalytic properties of gold nanoparticles are determined by their electronic and geometric structures. We revealed the geometries of several small neutral gold clusters in the gas phase by using vibrational spectroscopy between 47 and 220 wavenumbers. A two-dimensional structure for neutral Au₇ and a pyramidal structure for neutral Au₂₀ can be unambiguously assigned. The reduction of the symmetry when a corner atom is cut from the tetrahedral Au₂₀ cluster is directly reflected in the vibrational spectrum of Au₁₉.

Haruta *et al.*'s finding that dispersed gold nanoparticles show pronounced catalytic activity toward the oxidation of CO has triggered a gold rush in cluster chemistry (1). Although bulk gold is a classic example of chemical inertness (2), many later studies have confirmed the size-dependent reactivity of deposited gold clusters (3–6). Small particles of gold differ from the bulk because they contain edge atoms that have low coordination (7) and can adopt binding geometries that lead to a more reactive electronic structure (8). Thus, the secret of the catalytic properties of gold nanoparticles lies at least partly in their geometric

structure. Structural information for deposited gold mono- and bilayers on titania has been obtained by using high-resolution electron energy-loss spectroscopy on CO adsorbates (9). Determining the three-dimensional (3D) structure of deposited gold nanoparticles is more challenging, but recently has been achieved for clusters containing around 310 atoms by means of aberration-corrected scanning transmission electron microscopy (10).

The geometry of nanoparticles can also be studied in the gas phase. The advantages of this approach are the exact knowledge of the clusters' size and the absence of any interaction with the

surrounding environment. The properties of such well-defined species can thus be modeled very precisely with quantum-mechanical calculations. Different experimental techniques exist for the study of free clusters. By measuring the mobility of size-selected gold anions and cations in helium, a transition from 2D to 3D structures has been found (11, 12). This transition appears at different cluster sizes for cations and anions and is yet to be determined experimentally for neutral species. A combination of photoelectron spectroscopy and quantum-mechanical calculations has revealed fascinating structures of anionic gold species—for example, cages for clusters containing 16 to 18 atoms (13), a tetrahedral pyramid for Au₂₀⁻ (14), and a possibly chiral structure for Au₃₄⁻ (15). These structural motifs have been confirmed by measurement of the electron diffraction pattern of size-selected trapped anions (15, 16). Although ion mobility measurements, photoelectron spectroscopy

¹Fritz-Haber-Institut der Max-Planck-Gesellschaft, 14195 Berlin, Germany. ²Steele Institute for Molecular Sciences, Ottawa, Ontario K1A 0R6, Canada. ³Stichting voor Fundamenteel Onderzoek der Materie (FOM) Institute for Plasma Physics Rijnhuizen, 3439 MN Nieuwegein, Netherlands.

*To whom correspondence should be addressed. E-mail: fielicke@fhi-berlin.mpg.de